IOP PUBLISHING PLASMA PHYSICS AND CONTROLLED FUSION

Plasma Phys. Control. Fusion **50** (2008) 115001 (24pp) doi:10.1088/0741-3335/50/11/115001

Design and simulation of extremum-seeking open-loop optimal control of current profile in the DIII-D tokamak

Y Ou[1], C Xu[1], E Schuster[1], T C Luce[2], J R Ferron[2], M L Walker[2] and D A Humphreys[2]

[1] Lehigh University, Bethlehem, PA 18015 USA
[2] General Atomics, San Diego, CA 92186 USA

E-mail: yoo205@lehigh.edu

Received 11 January 2008, in final form 1 July 2008
Published 17 September 2008
Online at stacks.iop.org/PPCF/50/115001

Abstract

In a magnetic fusion reactor, the achievement of a certain type of plasma current profiles, which are compatible with magnetohydrodynamic stability at high plasma pressure, is key to enable high fusion gain and non-inductive sustainment of the plasma current for steady-state operation. The approach taken toward establishing such plasma current profiles at the DIII-D tokamak is to create the desired profile during the plasma current ramp-up and early flattop phases. The evolution in time of the current profile is related to the evolution of the poloidal flux, which is modeled in normalized cylindrical coordinates using a partial differential equation usually referred to as the magnetic diffusion equation. The control problem is formulated as an open-loop, finite-time, optimal control problem for a nonlinear distributed parameter system, and is approached using extremum seeking. Simulation results, which demonstrate the accuracy of the considered model and the efficiency of the proposed controller, are presented.

(Some figures in this article are in colour only in the electronic version)

1. Introduction

The need to optimize the tokamak concept for the design of an economical, possibly steady-state, fusion power plant has motivated extensive international research aimed at finding the so-called advanced tokamak (AT) operational scenarios [1]. Such regimes are characterized by a high confinement state with improved magnetohydrodynamic (MHD) stability, which yields a strong improvement of the plasma performance quantified by the increase in the energy confinement time and plasma pressure. In such conditions a dominant fraction of the plasma current is the self-generated bootstrap current, and the requirement on externally driven current for steady-state operation is reduced.

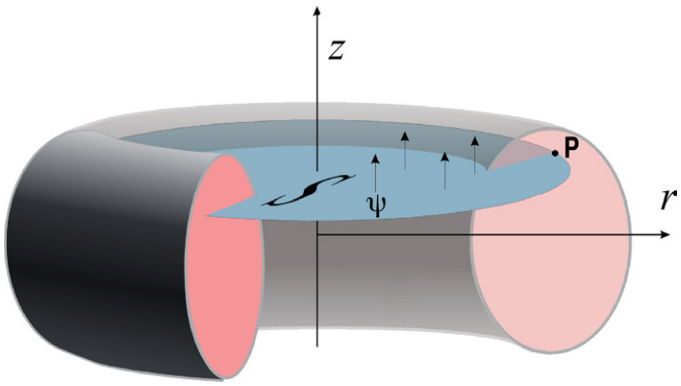

Figure 1. Poloidal flux in a tokamak.

Setting up a suitable current profile, characterized by a weakly reversed magnetic shear, has been demonstrated to be a key condition for one possible advanced scenario with improved confinement and possible steady-state operation [2–4]. It has been demonstrated that simultaneous real-time control of the current and pressure profiles could lead to the steady-state sustainment of an internal transport barrier (ITB), and so to a stationary optimized plasma regime. It has also been suggested that global current profile control, eventually combined with pressure profile control, can be an effective mechanism for neoclassical tearing mode (NTM) control and avoidance. A key goal in control of an AT discharge is to maintain current and pressure profiles that are compatible with both MHD stability at high toroidal beta and at a high fraction of the self-generated bootstrap current. This will enable high fusion gain and increase the fraction of non-inductive current for steady-state operation.

It is possible to use the poloidal component of the helicoidal magnetic lines to define nested toroidal surfaces corresponding to constant values of the poloidal magnetic flux. As is illustrated in figure 1, the poloidal flux ψ at a point P in the (r, z) cross section of the plasma (i.e. poloidal cross section) is the total flux through the surface S bounded by the toroidal ring passing through P, i.e. $\psi = \int B_{\mathrm{pol}}\,\mathrm{d}S$. The safety factor q is a measure of the pitch of the helicoidal magnetic field line lying on the magnetic surface, i.e. of the relation between the toroidal and the poloidal components of the helicoidal magnetic field line, $q = \mathrm{d}\Phi/\mathrm{d}\psi$. In a tokamak discharge, the toroidal field (TF) coils are operated so as to produce an approximately constant TF. Thus, the q profile is considered in most cases to be a function of the variable poloidal field (PF), or equivalently of the poloidal flux, i.e. $q = q(\psi)$. When the plasma shape is controlled at steady-state equilibrium, the PF coil currents are nearly constant. Therefore, changes in the PF, and therefore in the poloidal flux ψ, are dominated by changes in the spatial distribution of the plasma toroidal current density (the current profile). Through this chain of dependences, it can be seen that the safety factor q profile depends on the current profile (and vice versa). Thus, many physicists speak interchangeably of the current profile and the q-profile. Another quantity related to q is its inverse, known as the rotational transform $\iota(\psi) = 1/q(\psi)$. It can be shown that $\iota(\psi)$ is proportional to the total current inside the flux surface represented by the poloidal flux value ψ.

Recent experiments in different devices around the world (JET, DIII-D, JT-60U [5], Tore Supra [6, 7]) have demonstrated significant progress in achieving profile control. At JET, different current and temperature gradient target profiles have been reached and sustained for several seconds during the flattop current phase [3, 4]. The control scheme relies on

the experimental identification of a linearized static response model, using lower hybrid current drive (LHCD), ion cyclotron resonance heating (ICRH) and neutral beam injection (NBI) as actuators. The controller, which finally reduces to a proportional-integral regulation incorporating information of the static response of the system, has been shown effective when rapid plasma events are absent. If the controller is expected to respond to rapid transients, such as MHD phenomena, which may displace the system on a short timescale during the slow evolution of the current density profile toward its desired shape, information of the dynamic response of the system must be incorporated into the controller synthesis. Exploiting the different time scales of kinetic and magnetic variables, a dynamic model has recently been identified at JET and used for the synthesis of a two-time-scale controller [8]. In contrast to the JET approach, experiments at DIII-D focus on creating the desired q profile during the plasma current ramp-up and early flattop phases with the aim of maintaining this target profile during the subsequent phases of the discharge. Active feedback control of the evolution of $q(0)$ and $q_{\min}$ during the initial phase of the discharge has already been demonstrated at DIII-D [9, 10] changing the plasma conductivity through electron heating, and therefore modifying the rate of relaxation of the current profile. The q profile is obtained in real time from a complete equilibrium reconstruction using data from the motional stark effect (MSE) diagnostic. The controller requests a power level to the actuator (electron cyclotron heating (ECH) or neutral beam heating (NBH)) which is equal to preprogrammed feed-forward value plus the error in q times a proportional gain (P controller). Present limitations of this controller (oscillations and instability), the high dimensionality of the problem and the strong coupling between the different variables describing the dynamics of the current profile of the plasma motivate the design of a model-based, multi-variable controller that takes into account the dynamics of the q response to the different actuators. Since the actuators that are used to achieve the desired target profile are constrained by physical limitations, experiments have shown that some of the desirable target profiles may not be achieved for all arbitrary initial conditions. Therefore, a perfect matching of the desirable target profile may not be physically possible. In practice, the objective is to achieve the best possible approximate matching in a short time window $[T_1, T_2]$ during the early flattop phase of the total plasma current pulse, as shown in figure 2. Thus, such a matching problem can be treated as an optimal control problem for a nonlinear partial differential equation (PDE) system.

Extremum seeking [11] is employed in this work to tackle a finite-time optimal control problem for a nonlinear, distributed-parameter system. Extremum seeking is applicable to systems where the input-to-output map, possible nonlinear, is unknown but has an extremum. The objective of the extremum seeking algorithm is to find the set of input parameters that achieve the extremum. In this work, we use extremum seeking to obtain the evolutions of the control inputs in the time interval $[0, T]$ that minimize the quadratic error between the actual current profile at time $T \in [T_1, T_2]$ and a desired target profile. This work is aimed at saving long trial-and-error periods of time currently spent by fusion experimentalists trying to manually adjust the time evolutions of the actuators to achieve the desired current profile at sometime $T \in [T_1, T_2]$ during the early stage of the flattop phase.

This paper is organized as follows. In section 2, the control-oriented dynamic model for the poloidal flux evolution during the inductive phase used for control design is described. In addition, a comparison between the response of the proposed dynamic model and experimental data from DIII-D is provided. However, as will become clear during the presentation of the results, the proposed control approach does not depend on this particular model, and more complex and accurate models can be used. Section 3 describes the control objectives during the different phases of the discharge. An open-loop control approach based on extremum seeking is introduced in section 4. A simulation study showing the effectiveness of the extremum

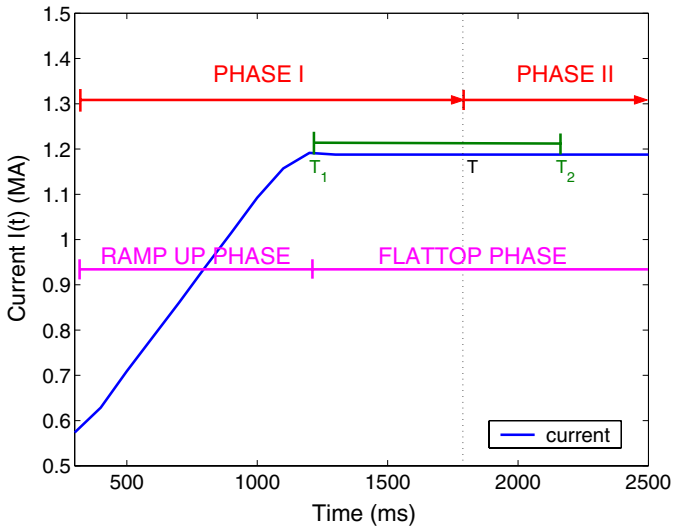

Figure 2. The total plasma current evolution can be roughly divided into two phases: the ramp-up phase and the flattop phase. The control problem focuses on phase I that includes the ramp-up phase and the first part of the flattop phase. The control goal is to drive the magnetic flux profile from some initial arbitrary condition to a predefined target profile at some time T between the time window $[T_1, T_2]$, which is in the flattop phase.

seeking optimal control method is presented in section 5. Finally, conclusions and identified future work are presented in section 6.

2. Current profile evolution model

2.1. Control-oriented dynamic model

With the ultimate goal of enabling model-based active control of the current profile at DIII-D, particularly in closed-loop, a control-oriented model for the dynamic evolution of the poloidal flux profile during and just following the ramp-up of the plasma current has recently been proposed [12]. The magnetic diffusion equation is combined with empirical correlations obtained at DIII-D for the temperature and non-inductive current to introduce a simplified dynamic model describing the evolution of the poloidal flux, and therefore the q profile, during the inductive phase of the discharge.

The model makes the simplifying assumption that the magnetic geometry is fixed in time. This excludes two potential sources of flux—a change in ρ_b (either by a change in the shape of the last closed flux surface or in $B_{\phi,o}$) and a change in location of the geometric center of the interior flux surfaces relative to that of the last closed flux surface. Changes in ρ_b are small by design in the experiments of interest, but it is straightforward to include this effect in the model for situations where it would be important. Changes in the relative positions of the flux surfaces do occur, but for cases of interest, these happen slowly enough and they can be neglected.

The current density j, which flows toroidally around the tokamak and whose profile must be controlled, is related to derivatives of the poloidal magnetic flux ψ with respect to the toroidal magnetic flux Φ. We let ρ be an arbitrary coordinate indexing the magnetic surface. Any quantity constant on each magnetic surface could be chosen as the variable ρ. We choose

Table 1. Description of the parameters.

Parameters	Description
ψ	Poloidal flux
η	Plasma resistivity
T_e	Electron temperature
n	Plasma density
$\mu_o = 4\pi \times 10^{-7}\,\frac{H}{m}$	Vacuum permeability
$\rho_b = 0.79\,m$	Radius of last closed flux surface
Φ_b	Toroidal flux in the last closed flux surface
$B_{\phi,o} = 1.85\,T$	Reference magnetic field at R_o
$R_o = 1.67\,m$	Reference point for $B_{\phi,o}$ (e.g. geometric center of plasma R_{geo})
$\hat{\rho}$	Normalized radius $\frac{\rho}{\rho_b}$
$\hat{F}, \hat{G}, \hat{H}$	Geometric factors (functions of $\hat{\rho}$ (figure 3))
$\bar{j}_{NI}$	Any non-inductive source of current density (neutral beam, electron cyclotron, etc)
$\langle\rangle$	Flux-surface average
j	Toroidal current density
E	Toroidal electric field
$\sigma = 1/\eta$	Plasma conductivity
I	Total plasma current
P_{tot}	Total power of non-inductive current drives
$\bar{n}$	Spatially average density

the mean geometric radius of the magnetic surface as the variable ρ, i.e. $\pi B_{\phi,o}\rho^2 = \Phi$. The variable $\hat{\rho}$ denotes the normalized radius ρ/ρ_b, and ρ_b is the radius of last closed flux surface. The evolution of the poloidal flux in normalized cylindrical coordinates is given by the magnetic diffusion equation,

$$\frac{\partial\psi}{\partial t} = \frac{\eta(T_e)}{\mu_o\rho_b^2\hat{F}^2}\frac{1}{\hat{\rho}}\frac{\partial}{\partial\hat{\rho}}\left(\hat{\rho}\hat{F}\hat{G}\hat{H}\frac{\partial\psi}{\partial\hat{\rho}}\right) - R_o\hat{H}\eta(T_e)\frac{\langle\bar{j}_{NI}\cdot\bar{B}\rangle}{B_{\phi,o}}, \tag{1}$$

where all the parameters are defined in table 1. The boundary conditions of (1) are given by

$$\begin{aligned}\left.\frac{\partial\psi}{\partial\hat{\rho}}\right|_{\hat{\rho}=0} &= 0,\\ \left.\frac{\partial\psi}{\partial\hat{\rho}}\right|_{\hat{\rho}=1} &= \frac{\mu_o}{2\pi}\frac{R_o}{\hat{G}|_{\hat{\rho}=1}\hat{H}|_{\hat{\rho}=1}}I(t),\end{aligned} \tag{2}$$

where $I(t)$ denotes the total plasma current.

During 'phase I' (see figure 2), mainly governed by the ramp-up phase, the plasma current is mostly driven by induction. In this case, it is possible to decouple the equation for the evolution of the poloidal flux from the evolution equations for the temperature $T_e(\hat{\rho}, t)$. Highly simplified models for the temperature and non-inductive toroidal current density are chosen for this phase. Based on experimental observations at DIII-D, the shapes of the profiles are assumed to remain fixed and equal to the so-called reference profiles, which are identified from DIII-D discharges associated with the experiment of interest. The responses to the actuators are simply scalar multiples of the reference profiles. We consider the line average density $\bar{n}(t)$, the plasma current $I(t)$ and the total power of the non-inductive current sources (ECH, NBH, etc.) $P_{tot}(t)$ as the physical actuators of the system.

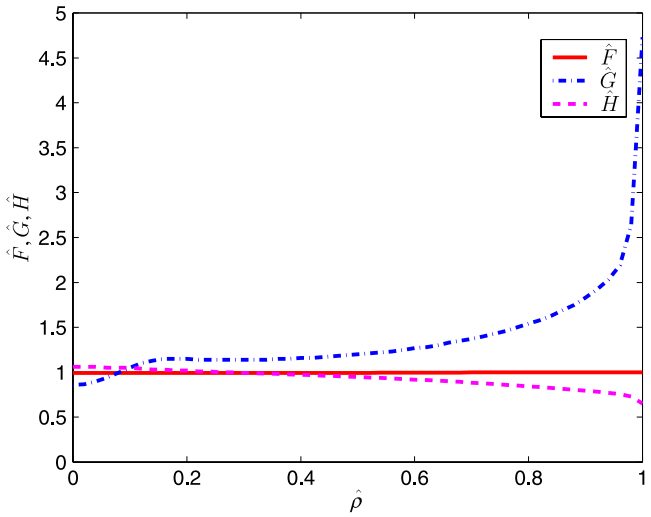

Figure 3. Geometric factors $\hat{F}$, $\hat{G}$ and $\hat{H}$.

The temperature T_e is assumed proportional to $I(t)\sqrt{P_{tot}}/\bar{n}(t)$, and can be written as

$$T_e(\hat{\rho}, t) = k_{T_e} T_e^{\text{profile}}(\hat{\rho}) \frac{I(t)\sqrt{P_{tot}}}{\bar{n}(t)}, \tag{3}$$

where the reference profile T_e^{profile} identified from DIII-D through Thomson scattering is given in figure 4, and $k_{T_e} = 1.7295 \times 10^{10}\,\text{m}^{-3}\,\text{A}^{-1}\,\text{W}^{-1/2}$. The average density $\bar{n}$ is defined as

$$\bar{n}(t) = \int_0^1 n(\hat{\rho}, t)\,\text{d}\hat{\rho}, \tag{4}$$

where n denotes the plasma density.

The non-inductive toroidal current density $\langle \bar{j}_{NI} \cdot \bar{B} \rangle / B_{\phi,o}$ is assumed to follow

$$\frac{\langle \bar{j}_{NI} \cdot \bar{B} \rangle}{B_{\phi,o}} = k_{NI\,par} j_{NI\,par}^{\text{profile}}(\hat{\rho}) \frac{I(t)^{1/2} P_{tot}(t)^{5/4}}{\bar{n}(t)^{3/2}}, \tag{5}$$

where the reference profile $j_{NI\,par}^{\text{profile}}$ identified from DIII-D through a combination of MSE diagnostics and the EFIT equilibrium reconstruction code [13, 14] is given in figure 4, and $k_{NI\,par} = 1.2139 \times 10^{18}\,\text{m}^{-9/2}\,\text{A}^{-1/2}\,\text{W}^{-5/4}$.

The model for T_e and $\langle \bar{j}_{NI} \cdot \bar{B} \rangle / B_{\phi,o}$ presented above considers neutral beams as the only source of current and heating. In the case where more heating and current sources are considered, equations (3) and (5) should include the weighted contributions of the different sources, and reference profiles need to be identified for each heating and current source.

The resistivity η scales with the temperature T_e as

$$\eta(\hat{\rho}, t) = \frac{k_{\text{eff}} Z_{\text{eff}}}{T_e^{3/2}(\hat{\rho}, t)}, \tag{6}$$

where $Z_{\text{eff}} = 1.5$ and $k_{\text{eff}} = 4.2702 \times 10^{-8}\,\Omega\,\text{m(keV)}^{3/2}$. The total current density is given by

$$j = \frac{1}{\mu_0 \rho_b^2 \hat{F}^2 \hat{H} \hat{\rho}} \frac{\partial}{\partial \hat{\rho}} \left(\hat{\rho} \hat{F} \hat{G} \hat{H} \frac{1}{R_0} \frac{\partial \psi}{\partial \hat{\rho}} \right). \tag{7}$$

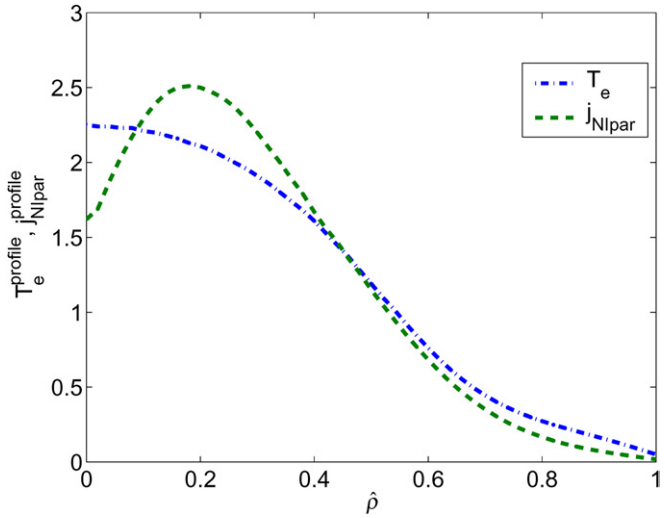

Figure 4. Temperature ($T_{\mathrm{e}}^{\mathrm{profile}}$ (keV)), and non-inductive toroidal current density ($j_{\mathrm{NI\,par}}^{\mathrm{profile}}$ (10^5 A m^{-2})) reference profiles identified from experimental shot 119566.

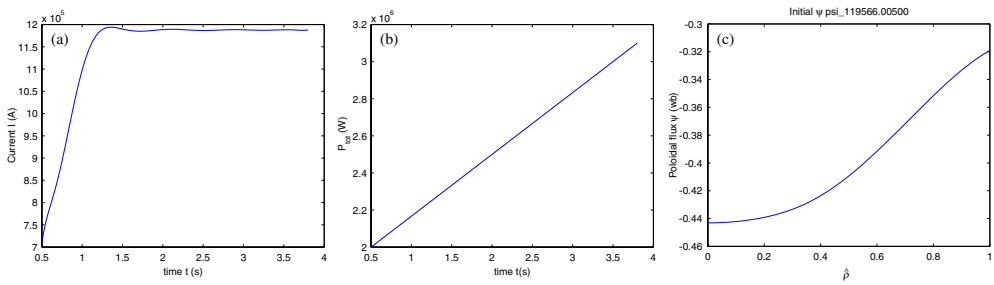

Figure 5. (*a*) Current $I(t)$ evolution, (*b*) Total power $P_{\mathrm{tot}}(t)$ evolution, (*c*) Initial ψ profile extracted from experimental shot 119566.

2.2. Dynamic response of inductive-phase model

The system of equations describing the poloidal flux evolution has been successfully implemented in a numerical solver. In this simulation example we consider the time interval [0.5 s, 3.8 s]. The plasma current $I(t)$ is shown in figure 5(*a*), the total power $P_{\mathrm{tot}}(t)$ is depicted in figure 5(*b*) and the average density is scaled with the current, i.e. $\bar{n}(t)(10^{19}\,\mathrm{m}^{-3}) = 3I(t)$ (MA). The initial poloidal flux profile ψ extracted from shot 119566 is shown in figure 5(*c*). Figure 6 shows the profile evolutions for the poloidal flux ψ, the total current density j, the electron temperature T_{e}, the parallel non-inductive current $\langle \bar{j}_{\mathrm{NI}} \cdot \bar{B} \rangle / B_{\phi,\mathrm{o}}$, the conductivity σ and the driving term $I(t)^{1/2} P_{\mathrm{tot}}(t)^{5/4} \bar{n}(t)^{-3/2}$, based on the dynamic model (1)–(7). As expected, the area under the current density curve increases with time, consistent with the boundary condition related to the total current at $\hat{\rho} = 1$ and the current $I(t)$ evolution shown in figure 5(*a*). The maximum of the current density moves slowly toward a smaller radius, as expected from a diffusive process. Given the three order of magnitude variation in the plasma conductivity ($\sim T_{\mathrm{e}}^{3/2}$, large in the hot center and small at the cold edge), the current density rapidly equilibrates at the edge, but evolves much more slowly in the center. The T_{e} profile

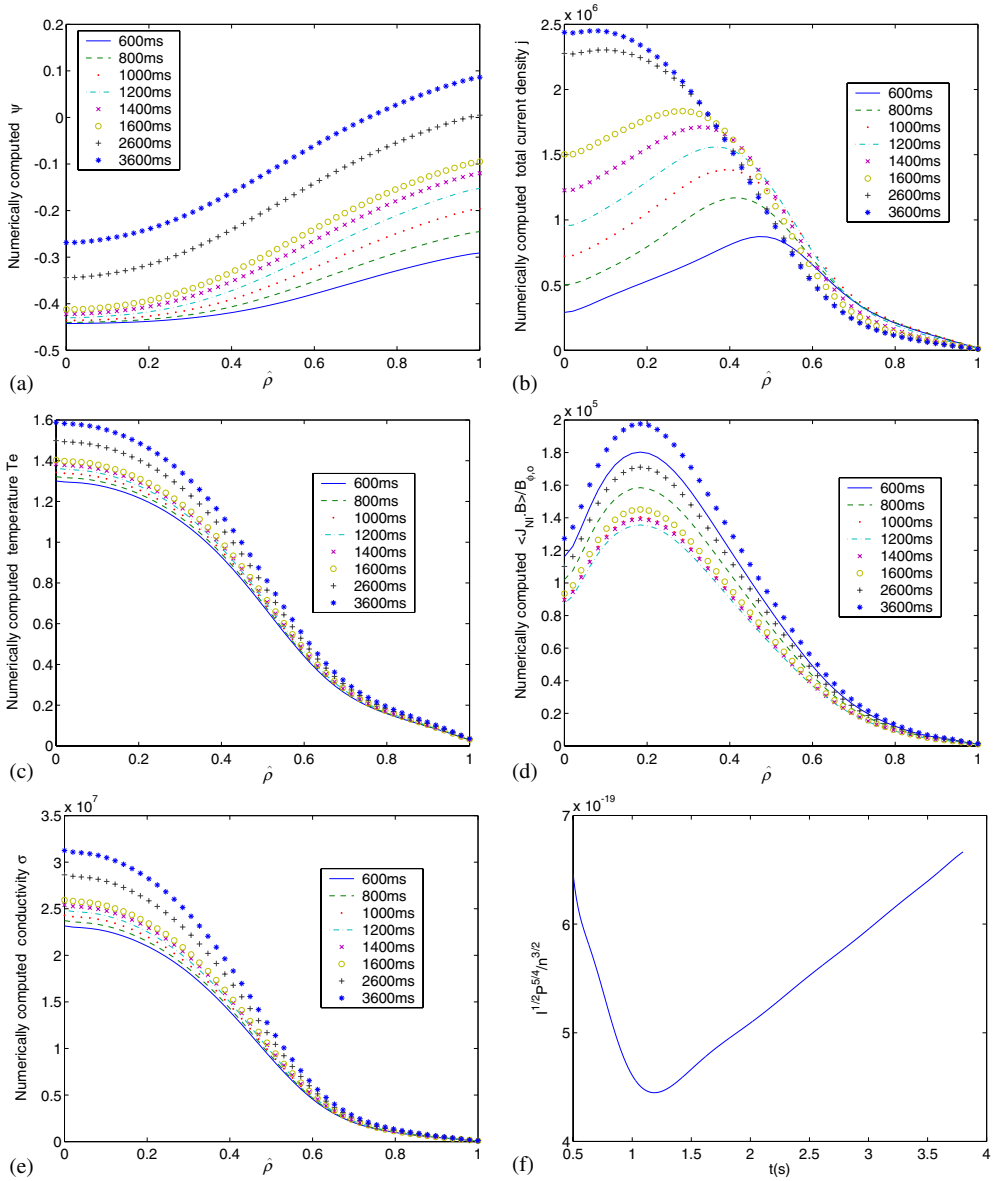

Figure 6. Profile evolutions in a simulated 'discharge': (*a*) ψ (Wb), (*b*) j (A m^{-2}), (*c*) T_e (keV), (*d*) $\langle \bar{j}_{\rm NI} \cdot \bar{B} \rangle / B_{\phi,\rm o}$ (A m^{-2}), (*e*) σ (Ω m^{-1}), (*f*) $I(t)^{1/2} P_{\rm tot}(t)^{5/4} \bar{n}(t)^{-3/2}$ (A$^{1/2}$ W$^{5/4}$ m$^{9/2}$).

grows monotonically since $I(t)\sqrt{P_{\rm tot}}\bar{n}(t)^{-1} \sim \sqrt{P_{\rm tot}}$ in this simulation case (see figure 5(*b*)). The $\langle \bar{j}_{\rm NI} \cdot \bar{B} \rangle / B_{\phi,\rm o}$ profile evolution follows the driving term $I(t)^{1/2} P_{\rm tot}(t)^{5/4} \bar{n}(t)^{-3/2}$. The simulated profile evolutions show qualitative agreement with tokamak experiments.

2.3. Comparisons with experimental results

Experimental validation of the simplified, control-oriented model has already started. We now present initial comparison results. This comparison does not intend to be exhaustive but

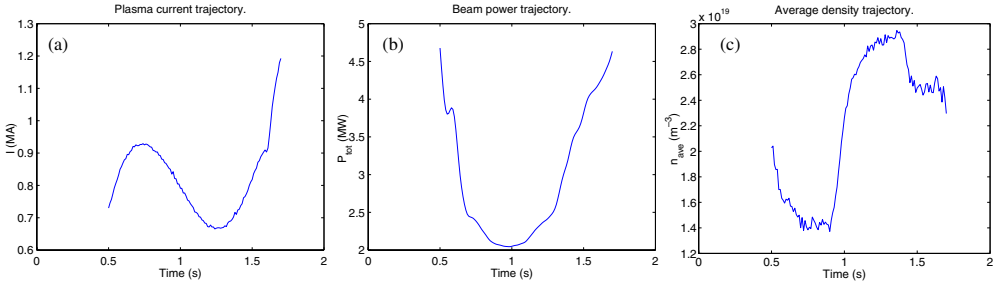

Figure 7. Actuator waveforms used in comparison (*a*) $I(t)$, (*b*) P_{tot}, (*c*) $\bar{n}(t)$.

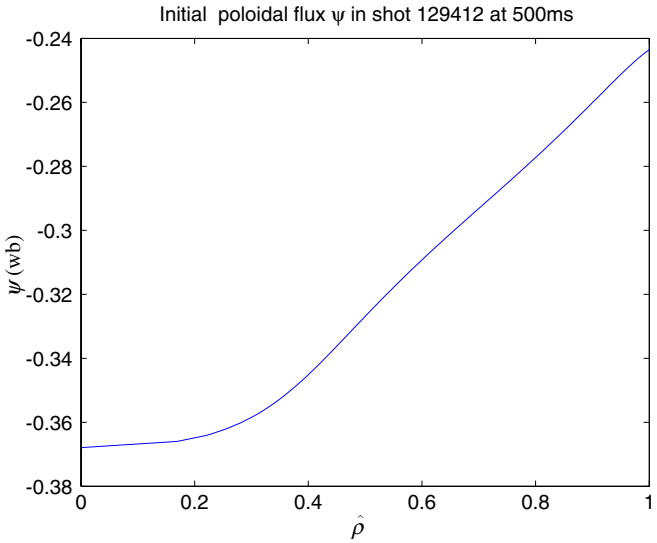

Figure 8. Initial ψ profile extracted from shot 129412 at 500 ms.

focuses on one specific case of interest. The proposed dynamic model is compared with DIII-D shot 129412, which was run by reproducing 129400 until 500 ms, then turning off the electron cyclotron current drive (ECCD), and from that point on controlling the plasma current, line average density and beam power as shown in figure 7.

Figure 8 illustrates the poloidal flux ψ at 500 ms for shot 129412, which is considered the initial poloidal flux profile for the simulation study. Figures 9 and 10 show, respectively, the simulated and experimental poloidal flux ψ evolving from 0.5 s to 1.7 s. Figures 11 and 12 compare simulated and experimental poloidal fluxes ψ and safety factors q at 1.7 s.

Figures 13 and 14 show, respectively, the experimental and simulated electron temperature profiles at different times in the interval 0.5 s–1.7 s. Although the differences are significant in the electron temperature profiles because the profiles extracted from shot 119566 do not seem appropriate to model shot 129412, the trend of the proposed scaling with the actuators has been successfully validated. To illustrate this point the term $I(t)\sqrt{P_{\text{tot}}}(t)/\bar{n}(t)$ in (3) is plotted in figure 15. It is possible to note that the temperature profile in figure 13, and in figure 14 as well, indeed follows the signal in figure 15 as predicted by the model. It is interesting to note that in spite of the poor matching between experiment and model for the electron temperature,

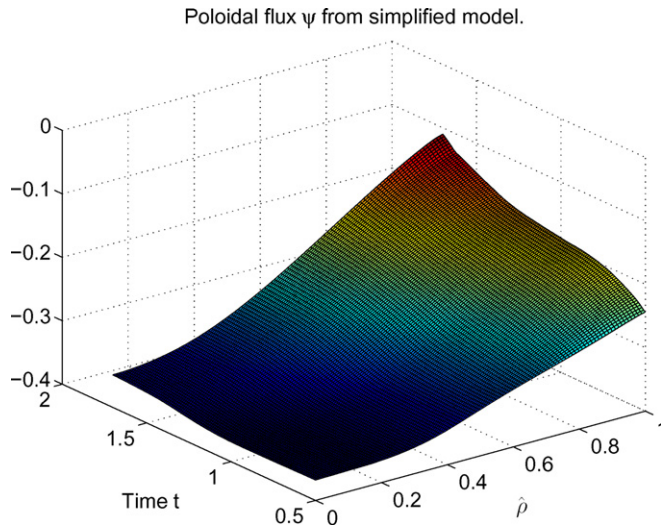

Figure 9. ψ (Wb) evolution predicted by simplified model.

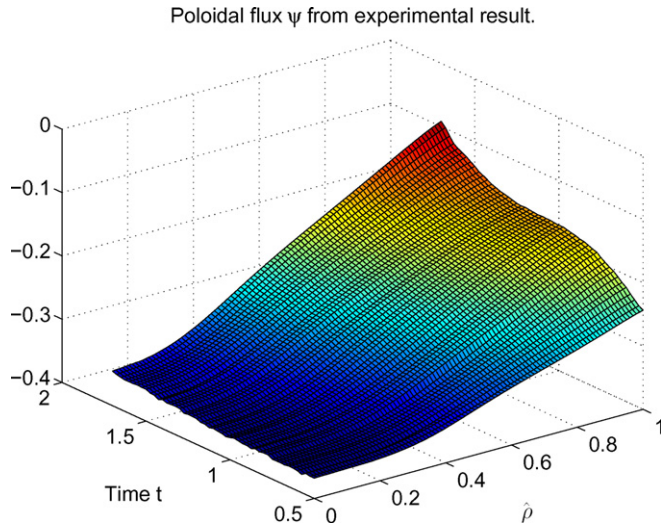

Figure 10. ψ (Wb) evolution in experimental shot 129412.

the simplified model seems to predict the evolution of the poloidal flux ψ, and therefore the q profile, accurately enough for control purposes as shown in figures 9–12.

A substantial experimental physics effort has been going on for several years to develop predictive models for evolution of poloidal flux, or equivalently, current profiles in toroidal plasmas. Our work draws on the result of those efforts but does not supersede it, since our purpose is simply the conversion of this accepted physics model to a form useful for control design. It is important to note that we are modeling for control and not for physical understanding and, consequently, the model needs only to capture the dominant effects of the system dynamics because one of the main characteristics of feedback is the ability to deal with model uncertainties. It is also important to emphasize that for the open-loop control design

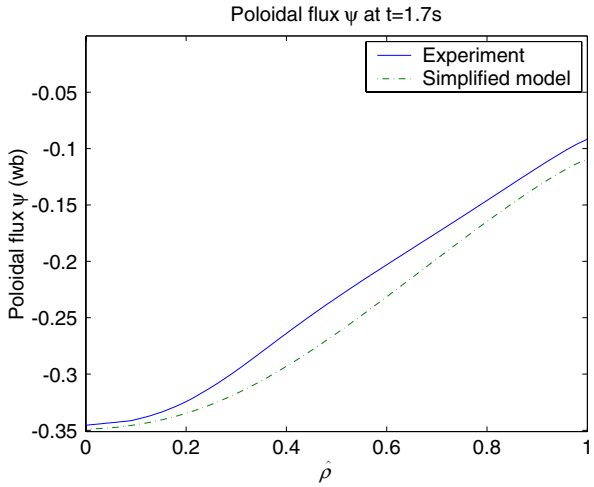

Figure 11. Comparison of poloidal flux ψ profiles at 1.7 s.

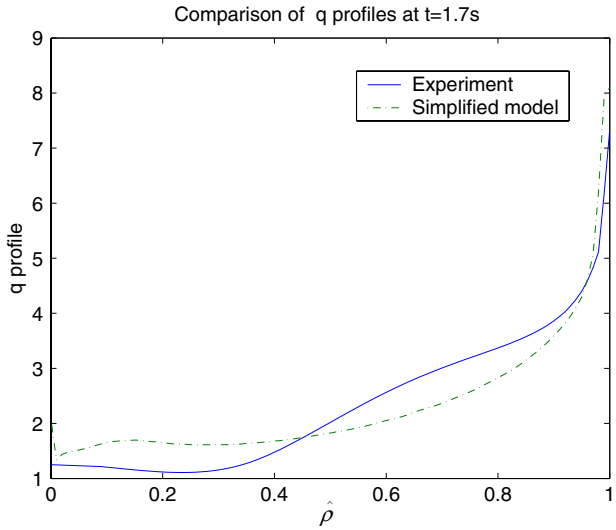

Figure 12. Comparison of q profiles at 1.7 s.

proposed in this paper full predictive codes (CORSICA, CRONOS, PTRANSP, etc) could be used with the potential of a more accurate prediction than that provided by the simplified control-oriented model described in section 2.1.

3. Control problem description

The control objective, as well as the dynamic models for current profile evolution, depend on the phases of the discharge (figure 2). During 'phase I' the control goal is to drive the current profile from any arbitrary initial condition to a prescribed target profile at some time $T \in [T_1, T_2]$ in the flattop phase of the total current $I(t)$ evolution. However, since the available actuators during

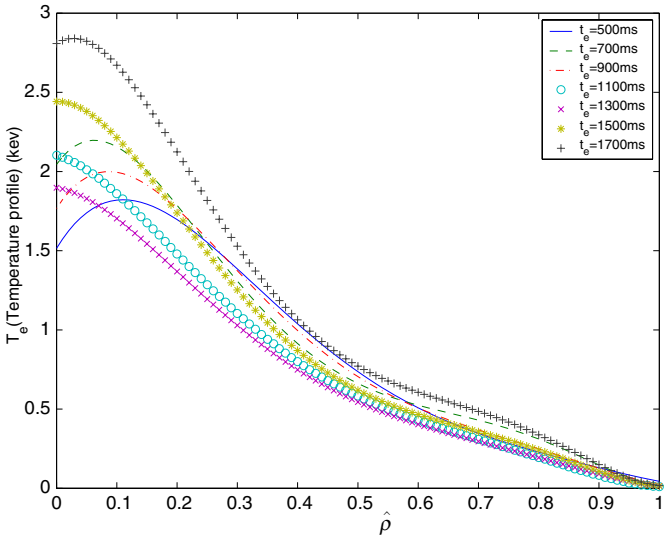

Figure 13. Temperature profiles obtained via Thomson scattering diagnostics for shot 129412.

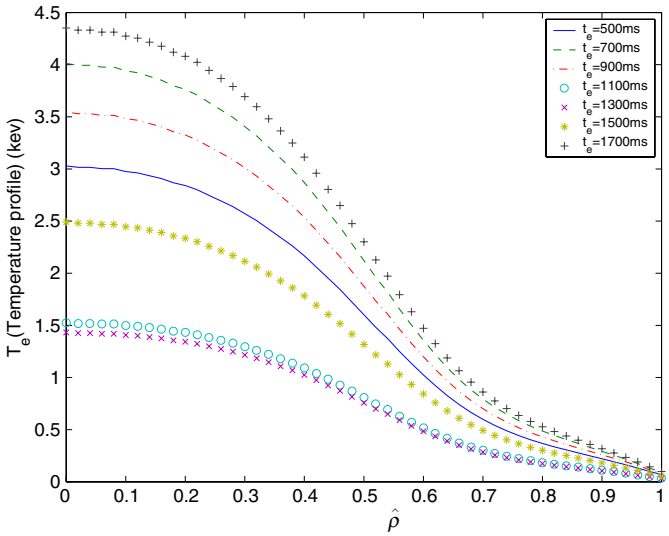

Figure 14. Temperature profiles predicted by the simplified model.

'phase I' differ from those used during 'phase II' and are constrained by physical limitations, the prescribed target profile is not an equilibrium profile during 'phase I'. During 'phase II' the control goal is to regulate the current profile using as little control effort as possible because the actuators are not only limited in power but also in energy. For this reason, the goal during 'phase I' is to set up an initial profile for 'phase II' as close as possible to its desirable profile.

In this paper, we focus on 'phase I'. It is important to note that although T_1 and T_2 can be adjusted as functions of the properties of the system, such as time scale and efficiency of the actuators, due to the nonlinearities of the system and the constraint of the actuators there is no guarantee that the target profile can indeed be reached within the time window $[T_1, T_2]$.

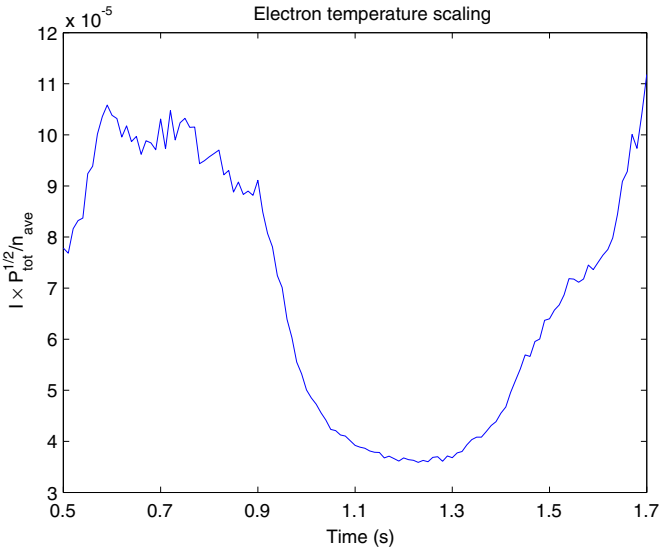

Figure 15. Time evolution of $I(t)\sqrt{P_{\rm tot}}/\bar{n}(t)$ (A W$^{1/2}$ m^3) for shot 129412.

Therefore, an optimal control problem must be solved, where control laws $I(t)$, $P_{\rm tot}(t)$ and $\bar{n}(t)$ are sought to minimize the cost functional

$$J = \sqrt{\min_{t_j}(J^*(t_j))}, \tag{8}$$

where t_j are discrete points in time equally spaced within the interval $[T_1, T_2]$, e.g. $t(j) = T_1 = 1.2\,\text{s}, 1.3\,\text{s}, 1.4\,\text{s}, \ldots, T_2 = 2.4\,\text{s}$ for $j = 1, 2, 3, \ldots, 13$ and $J^*(t_j)$ is given by

$$J^*(t_j) = \frac{1}{N}\sum_{i=1}^{N}(\iota(\hat{\rho}_i, t_j) - \iota^{\rm des}(\hat{\rho}_i))^2, \tag{9}$$

where N is the number of discrete points in space within the interval [0, 1] for the normalized radius.

Since the rotational transform ι is proportional to the total current inside the flux surface represented by the poloidal flux value ψ, i.e. proportional to the spatial integral of the current density (7), the cost functional (8) has been defined in terms of this variable. The safety factor q and the rotational transform ι are related and defined as

$$\iota(\rho, t) = \frac{1}{q(\rho, t)} = \frac{\partial\psi(\rho, t)}{\partial\Phi}. \tag{10}$$

The constant relationship between Φ and ρ, $\rho = \sqrt{\Phi/\pi B_{\phi,\rm o}}$, and the definition of the normalized radius (in table 1) allow us to rewrite (10) as

$$\iota(\hat{\rho}, t) = \frac{\partial\psi}{\partial\hat{\rho}}\frac{1}{B_{\phi,\rm o}\rho_{\rm b}^2\hat{\rho}}, \tag{11}$$

where $B_{\phi,\rm o}$ and $\rho_{\rm b}$ are defined in table 1.

'Phase I' can be roughly divided into two phases, the ramp-up phase and the flattop phase. During the ramp-up phase, the three actuators $I(t)$, $\bar{n}(t)$ and $P_{\rm tot}(t)$ are assumed available for current profile control, whereas during part of the flattop phase ($t > T_1$) we choose to keep $I(t)$, $\bar{n}(t)$ and $P_{\rm tot}(t)$ fixed although modulation of these variables is possible. In addition

to these specific constraints during the flattop phase, the absolute values, and sometimes the derivatives in time, of the control variables must be within some specific limits during the whole 'phase I'. The physical ranges for $I(t)$, $\bar{n}(t)$ and $P_{\text{tot}}(t)$ are given by

$$\begin{aligned} &0 \leqslant I(t) \leqslant I_{\max}, \\ &\left|\frac{\mathrm{d}I(t)}{\mathrm{d}t}\right| \leqslant \mathrm{d}I_{\max}, \end{aligned} \tag{12}$$

$$\begin{aligned} &I(\mathrm{MA}) \leqslant \frac{\bar{n}(t)}{10^{19}} \leqslant 5I(\mathrm{MA}), \\ &\mathrm{d}n_{\min} \leqslant \frac{\mathrm{d}\bar{n}(t)}{\mathrm{d}t} \leqslant \mathrm{d}n_{\max}, \end{aligned} \tag{13}$$

$$P_{\min} \leqslant P_{\text{tot}}(t) \leqslant P_{\max}. \tag{14}$$

The lower and upper limits for the line average density in (13) is set to prevent density instabilities and disruptions. The upper limit is approximately half of the Greenwald limit at DIII-D. To accurately reproduce experimental discharges, we must add constraints for $I(t)$ and $\bar{n}(t)$ at the initial time of 'phase I', i.e.

$$\begin{aligned} &I(t = 0\,\mathrm{s}) = I_0, \\ &\bar{n}(t = 0\,\mathrm{s}) = \bar{n}_0. \end{aligned} \tag{15}$$

In addition, a value of the total current $I(t)$ is prescribed for the flattop phase, i.e.

$$I(t \geqslant T_1) = I_{\text{target}}. \tag{16}$$

In summary, the optimal control problem (8) must be solved taking into account that: (i) during the ramp-up phase and eventually early flattop phase ($0 \leqslant t \leqslant T_1$) we can manipulate the three actuators while obeying the physical constraints (12)–(15) (ii) during the flattop phase $I(t)$ is constrained by (16), and $\bar{n}(t)$ and $P_{\text{tot}}(t)$ must be equal to $\bar{n}(T_1)$ and $P_{\text{tot}}(T_1)$, respectively. We seek $I(t)$, $\bar{n}(t)$ and $P_{\text{tot}}(t)$ for $t \in [0, T]$ that makes $\iota(\hat{\rho}, T)$ as close as possible to the prescribed target profile $\iota^{\text{des}}(\hat{\rho})$ at some time $T \in [T_1, T_2]$. It is important to emphasize at this point that the waveforms for $I(t)$, $\bar{n}(t)$ and $P_{\text{tot}}(t)$ for $t \in [0, T]$ obtained by solving the optimal control problem (8) represent the desired values for these controlled variables. The waveforms generated by the optimization algorithm (see section 4) are indeed the references for the controllers associated with the plasma current $I(t)$, line averaged density $\bar{n}(t)$ and beam power $P_{\text{tot}}(t)$. For instance, in the case of the plasma current, a PID loop regulates the ohmic coil voltage at DIII-D to make the plasma current measured by a Rogowski loop (which includes both inductive and non-inductive current components) follow the desired waveform generated by the optimization algorithm. Similarly to the case of the plasma current, a PID loop regulates gas puffing and pumping to make the line averaged density measured by a CO_2 interferometer follow the optimal waveform. The power of the current drives is directly controlled by the power supplies associated with the drives. Recent experiments in DIII-D have shown the possibility of controlling both plasma current and beam power very accurately. However, the control of the evolution of the line average density appears as more challenging. In order to ensure that the desired waveforms for the controlled variables can indeed be achieved by the associated control loops, the physical constraints in (12)–(15) must be carefully chosen, particulary for the line average density.

It is worth noting that we can rewrite the equation for the evolution of the poloidal flux (1) as

$$\frac{\partial \psi}{\partial t} = f_1(\hat{\rho})u_1(t)\frac{1}{\hat{\rho}}\frac{\partial}{\partial \hat{\rho}}\left(\hat{\rho} f_4(\hat{\rho})\frac{\partial \psi}{\partial \hat{\rho}}\right) - f_2(\hat{\rho})u_2(t) \tag{17}$$

with boundary conditions

$$\left.\frac{\partial\psi}{\partial\hat{\rho}}\right|_{\hat{\rho}=0}=0, \qquad \left.\frac{\partial\psi}{\partial\hat{\rho}}\right|_{\hat{\rho}=1}=k_3u_3(t), \tag{18}$$

and where

$$f_1(\hat{\rho})=\frac{k_{\text{eff}}Z_{\text{eff}}}{k_{T_e}^{3/2}\mu_o\rho_b^2}\frac{1}{\hat{F}^2(\hat{\rho})(T_e^{\text{profile}}(\hat{\rho}))^{3/2}}, \qquad u_1(t)=\left(\frac{\bar{n}(t)}{I(t)\sqrt{P_{\text{tot}}}}\right)^{3/2}, \tag{19}$$

$$f_2(\hat{\rho})=R_o\hat{H}\mu_o\rho_b^2\hat{F}^2(\hat{\rho})k_{\text{NI par}}j_{\text{NI par}}^{\text{profile}}(\hat{\rho})f_1(\hat{\rho}), \qquad u_2(t)=\frac{\sqrt{P_{\text{tot}}(t)}}{I(t)}, \tag{20}$$

$$k_3=\frac{\mu_o}{2\pi}\frac{R_o}{\hat{G}|_{\hat{\rho}=1}\hat{H}|_{\hat{\rho}=1}}, \qquad u_3(t)=I(t), \tag{21}$$

$$f_4(\hat{\rho})=\hat{F}\hat{G}\hat{H}. \tag{22}$$

The control of the magnetic diffusion PDE (17) is unique in the sense that it admits control not only through $u_2(t)$ (interior control) and $u_3(t)$ (boundary control) but also through $u_1(t)$, which we name *diffusivity control* in this paper. As the experiment and the equilibrium change, and therefore the profiles in figures 3 and 4, the dependence of f_1, f_2 and f_4 on $\hat{\rho}$ will also change, but the structure of (17) and (18) will remain. Thus, it is important to understand the control challenges associated with this system.

4. Extremum seeking optimal control

Extremum seeking control, a popular tool in control applications in the 1940–50s, has seen a resurgence in popularity as a real-time optimization tool in different fields of engineering [11, 15, 16]. Aerospace and propulsion problems (formation flight [17]), combustion instabilities [18,19], flow control [20,21], compressor rotating stall [22], automotive problems (soft landing of electromagnetic valves [23]), heat transfer problems [24] and bioreactors [25] are among its applications. Extremum seeking is applicable in situations where there is a nonlinearity in the control problem, and the nonlinearity has a local minimum or a maximum. One possible source of this nonlinearity is the control objective itself, which is added to the system through a cost functional of an optimization problem. Extremum seeking can be used for tuning some parameters of the system in order to achieve an optimal value of the cost functional. The parameter space can be multidimensional.

By parametrizing the control laws for $I(t)$, $P_{\text{tot}}(t)$ and $\bar{n}(t)$ in terms of a set of parameters denoted by θ, we use extremum seeking in this work for iterative tuning of θ to make the quadratic error between $\iota(\hat{\rho}, T)$ and the prescribed target profile $\iota^{\text{des}}(\hat{\rho})$ as small as possible at some time $T\in[T_1, T_2]$, i.e. to solve the optimization problem defined by

$$\min_{\theta} J(\theta), \tag{23}$$

with J defined in (8). The number of parameters used to represent the control laws is indeed a choice of the designer, and at the same time a tradeoff between the accuracy of the parametrization and the convergence speed of the extremum-seeking optimizer. In this work, the vector parameter θ has been chosen to have 10 components given by

$$\begin{aligned}\theta=[&I(0.4\,\text{s}), I(0.8\,\text{s}), P_{\text{tot}}(0\,\text{s}), P_{\text{tot}}(0.4\,\text{s}), P_{\text{tot}}(0.8\,\text{s}),\\ &P_{\text{tot}}(1.2\,\text{s}), \bar{n}(0.3\,\text{s}), \bar{n}(0.6\,\text{s}), \bar{n}(0.9\,\text{s}), \bar{n}(1.2\,\text{s})].\end{aligned} \tag{24}$$

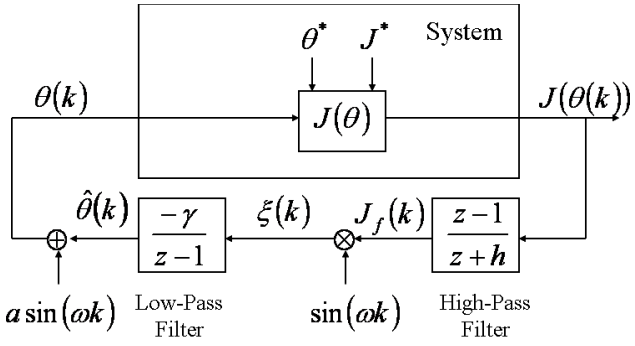

Figure 16. Extremum seeking control scheme.

We change or tune θ after each simulated plasma 'discharge'. Thus, we employ the discrete-time version [26] of extremum seeking. The implementation is depicted in figure 16, where z denotes the variable of the Z-transform [27]. The Z-transform plays the same role in discrete-time systems that the Laplace transform [28] plays in analysis of continuous-time systems. Given a sequence $u_0, u_1, \ldots, u_l, \ldots$, denoted as $\{u(l)\}$, and where l denotes the discrete time, its Z-transform is defined as

$$\mathcal{Z}\{u(l)\} = U(z) = \sum_{l=-\infty}^{l=\infty} u_l z^{-l}. \tag{25}$$

From this definition it is possible to note that

$$\mathcal{Z}\{u(l+1)\} = zU(z), \qquad \mathcal{Z}\{u(l-1)\} = z^{-1}U(z), \tag{26}$$

for which z is also called the time shift operator. The Z-transform permits the rapid conversion of a linear, constant-coefficient, difference equation in the discrete-time domain into a transfer function in the Z-domain, which is defined as the ratio of the Z-transform of the system output to the Z-transform of the system input. Therefore, the dynamics of a discrete-time linear system can be expressed either by a difference equation in the discrete-time domain or by a transfer function in the Z-domain.

The static nonlinear block $J(\theta)$ in figure 16 is assumed to have a minimum J^* at $\theta = \theta^*$. The purpose of the extremum seeking optimization algorithm is to use the gradient information of the static map $J(\theta)$ to drive θ to θ^* so that the cost functional $J(\theta)$ is driven to its minimum J^*. The variable $\hat{\theta}$ in figure 16 denotes the estimate of the unknown optimal parameter θ^* provided by the extremum seeking algorithm. The probing signal $a\sin(\omega t)$, with $a > 0$, added to the estimate $\hat{\theta}$ and fed into the plant helps to get a measure of the gradient information of the map $J(\theta)$. The high-pass filter preserves only the perturbation in the cost functional J caused by the perturbation in the θ parameter introduced by the probing signal. The demodulator picks the component of the filtered perturbed cost functional J_f with the same frequency ω as the probing signal. The resulting signal ξ, which can be seen as proportional to the gradient of the map $J(\theta)$, is used by the pure-integrator low-pass filter to update the θ parameter in order to drive the cost functional J closer to its minimum.

Once $\theta(k)$ is defined at each iteration k of the extremum seeking optimization algorithm, the output of the static map $J(k) = J(\theta(k))$ can be computed after the simulated 'discharge' associated with each extremum seeking iteration takes place. In a simulation environment, we understand by 'discharge' the integration of the PDE equation (1)–(2). With this purpose, the control laws for $I(t)$, $P_{\text{tot}}(t)$ and $\bar{n}(t)$ must be reconstructed from $\theta(k)$. The reconstruction

of each one of the control laws is carried out through an optimal polynomial interpolation that takes into account the constraints in value and rate defined for the control laws. As an example, we state below the optimal polynomial interpolation problem defined for the plasma current $I(t)$. Similar optimization problems are defined for the other control laws. We write the plasma current as a polynomial in time t, i.e.

$$I(t) = \sum_{i=0}^{n_{\text{fit}}^I} x_i t^{n_{\text{fit}}^I - i}, \tag{27}$$

where n_{fit}^I denotes the order of the fitting polynomial and x_i, for $i = 0, \ldots, n_{\text{fit}}^I$, are its coefficients. Recalling that θ_1 and θ_2 represent the value of plasma current determined by the extremum seeking algorithm at $t = 0.4$ s and $t = 0.8$ s, respectively, we denote $x = [x_0 \cdots x_{n_{\text{fit}}^I}]$ as the coefficient vector and define the cost functional

$$J_{\text{fit}}^I(x) = (I(t = 0.4\,\text{s}) - \theta_1)^2 + (I(t = 0.8\,\text{s}) - \theta_2)^2. \tag{28}$$

The optimal polynomial interpolation problem can then be written as

$$\min_x J_{\text{fit}}^I(x) \tag{29}$$

subject to the following constraints:

$$\begin{aligned} &I(t = 0\,\text{s}) = I_0, \\ &I(t = T_1) = I_{\text{target}}, \\ &|\text{d}I(t_i)/\text{d}t| \leqslant \text{d}I_{\max}, \\ &0 < I(t_i) < I_{\max}, \end{aligned} \tag{30}$$

where $t_i = 0, 0.1, 0.2, ..., 1.1, 1.2$.

After reconstructing the control laws for $I(t)$, $P_{\text{tot}}(t)$ and $\bar{n}(t)$, the PDE equation (1)–(2) is integrated and the simulated profile $\iota(\hat{\rho}, t)$ is obtained[3]. The output of the nonlinear static map, $J(k) = J(\theta(k))$, is then calculated by evaluating (8) and used to compute $\theta(k+1)$ according to the extremum seeking procedure in figure 16 or written equivalently as

$$J_{\text{f}}(k) = -hJ_{\text{f}}(k-1) + J(k) - J(k-1), \tag{31}$$

$$\xi(k) = J_{\text{f}}(k)\sin(\omega k), \tag{32}$$

$$\hat{\theta}(k+1) = \hat{\theta}(k) - \gamma\xi(k), \tag{33}$$

$$\theta(k+1) = \hat{\theta}(k+1) + a\sin(\omega(k+1)), \tag{34}$$

where $a > 0$ and $\omega > 0$ denote the amplitude and frequency of the probing signal, $0 < h < 1$ denotes the cutoff frequency of the high-pass filter and $\gamma > 0$ denotes the gain of the pure-integrator low-pass filter. Note that equations (31) and (33) are the difference-equation versions of the transfer functions for the high-pass and low-pass filters in figure 16.

We present in the appendix an elementary intuitive explanation of how the extremum seeking optimization algorithm works, including a discussion on the constraints on the design parameters a, ω, h and γ. A rigorous analysis can be found in [11, 26].

5. Simulation results

The extremum seeking optimization algorithm has been tested for numerous combinations of different initial ψ profiles and ι target profiles. In this section, we present some simulation

[3] Note that is perfectly possible to use a different, probably more accurate, model for the evolution of the poloidal flux profile instead of model (1)–(2). For instance, full predictive codes (CORSICA, CRONOS, PTRANSP, etc) can be used to predict the evolution of the poloidal flux profile.

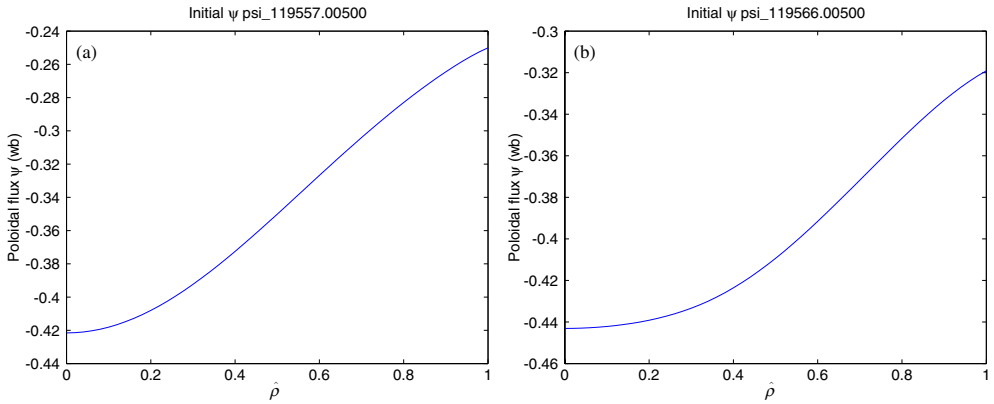

Figure 17. Initial ψ profile extracted from experimental shot 119557 (*a*), initial ψ profile extracted from experimental shot 119566 (*b*).

results showing the effectiveness of the extremum seeking controller designed to solve the optimal control problem (8) with $T_1 = 1.2\,\mathrm{s}$ and $T_2 = 2.4\,\mathrm{s}$. The simulations are carried out using 100 uniformly distributed spatial points and a sampling time of 10 ms over a time interval $[0, 2.4\,\mathrm{s}]$.

The optimal polynomial interpolation procedure described in section 4 is implemented in this section to reconstruct the control laws $I(t)$, $P_{\mathrm{tot}}(t)$ and $\bar{n}(t)$ from the optimized parameter vector $\theta(k)$ at each iteration k of the extremun seeking optimization algorithm. The current $I(t)$ is reconstructed in $[0, T_1]$ using constraint polynomial interpolation to fit the discrete points $I(t = 0) = I_0 \equiv 0.709\,\mathrm{MA}$, $I(t = 0.4\,\mathrm{s}) = \theta_1$, $I(t = 0.8\,\mathrm{s}) = \theta_2$, $I(t = T_1 = 1.2\,\mathrm{s}) = I_{\mathrm{target}} \equiv 1.188\,\mathrm{MA}$. In addition, $I(t) = I_{\mathrm{target}} \equiv 1.188\,\mathrm{MA}$ in $(T_1, T_2]$. The parameters $I_{\max} = 1.191\,\mathrm{MA}$ and $\mathrm{d}I_{\max} = 2\,\mathrm{MA\,s^{-1}}$ are used in (12) to evaluate the constraints for $I(t)$. The total power $P_{\mathrm{tot}}(t)$ is reconstructed using constrained polynomial interpolation to fit the discrete points $P_{\mathrm{tot}}(t = 0) = \theta_3$, $P_{\mathrm{tot}}(t = 0.4\,\mathrm{s}) = \theta_4$, $P_{\mathrm{tot}}(t = 0.8\,\mathrm{s}) = \theta_5$, $P_{\mathrm{tot}}(t = T_1 = 1.2\,\mathrm{s}) = \theta_6$. In addition, we make $P_{\mathrm{tot}}(t) = P_{\mathrm{tot}}(t = T_1 = 1.2\,\mathrm{s})$ for $t \in (T_1, T_2]$. The constraint for $P_{\mathrm{tot}}(t)$ is evaluated from (14) using $P_{\min} = 1\,\mathrm{MW}$ and $P_{\max} = 10\,\mathrm{MW}$. The line average density $\bar{n}(t)$ is obtained by constrained polynomial interpolation to fit the discrete points $\bar{n}(t = 0) = n_0 \equiv 2 \times 10^{19}\,\mathrm{m^{-3}}$, $\bar{n}(t = 0.3\,\mathrm{s}) = \theta_7$, $\bar{n}(t = 0.6\,\mathrm{s}) = \theta_8$, $\bar{n}(t = 0.9\,\mathrm{s}) = \theta_9$, $\bar{n}(t = T_1 = 1.2\,\mathrm{s}) = \theta_{10}$. For $t > T_1 = 1.2\,\mathrm{s}$, $\bar{n}(t) = \bar{n}(t = T_1 = 1.2\,\mathrm{s})$. The constraints for $\bar{n}(t)$ are given by (13) with $\mathrm{d}n_{\min} = -1.7 \times 10^{19}\,\mathrm{m^{-3}\ s^{-1}}$ and $\mathrm{d}n_{\max} = 3 \times 10^{19}\,\mathrm{m^{-3}\,s^{-1}}$.

The initial values for θ for all the simulation cases are arbitrarily chosen as follows:

$$\theta_{\mathrm{int}} = [0.94\,\mathrm{MA}, 1.16\,\mathrm{MA},$$
$$1.16\,\mathrm{MW}, 0.86\,\mathrm{MW}, 1.09\,\mathrm{MW}, 2.18\,\mathrm{MW},$$
$$1 \times 10^{19}\,\mathrm{m^{-3}}, 2 \times 10^{19}\,\mathrm{m^{-3}}, 3 \times 10^{19}\,\mathrm{m^{-3}}, 4 \times 10^{19}\,\mathrm{m^{-3}}].$$

The first simulation case considers the initial poloidal flux ψ shown in figure 17(*a*) and the monotonic target ι profile with positive shear near the axis shown in figure 18(*a*). Figure 18(*a*) compares the ι profile obtained by applying the extremum-seeking-based, optimal, open-loop control with the target ι profile. The small spatial scale structure in ι at a small radius is an artifact of the numerical scheme used to derive these variables from the calculated poloidal flux. Figure 18(*a*) also shows the evolution over time of the ι profile when the time evolutions

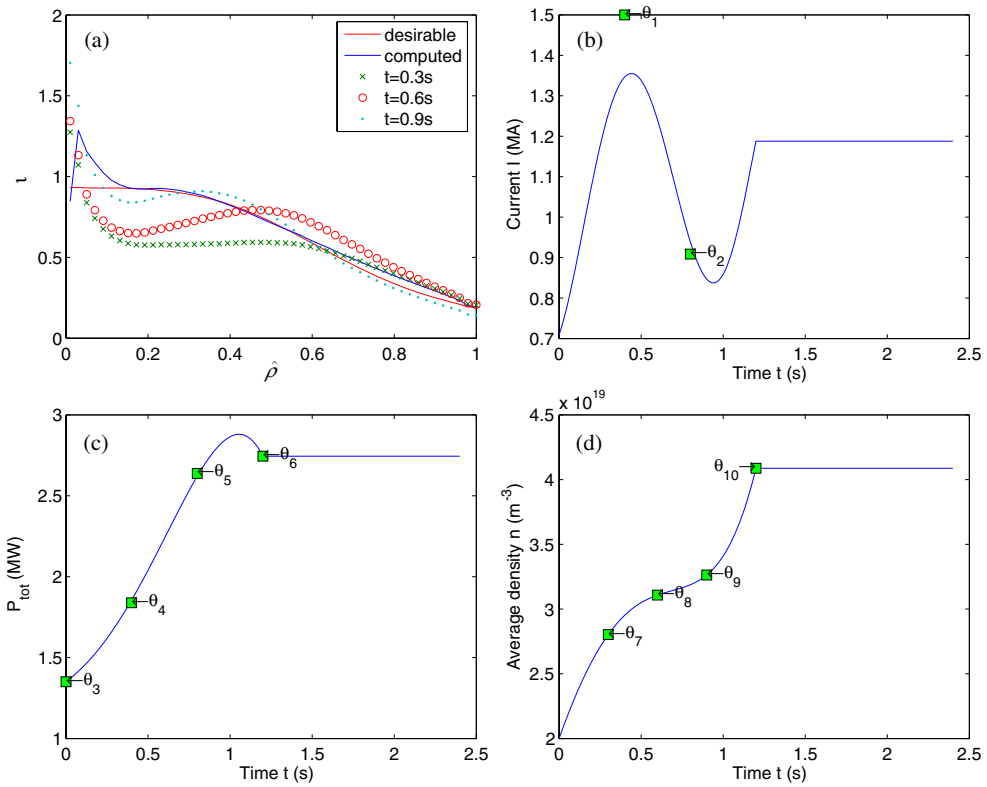

Figure 18. Simulation of extremum seeking optimal control: (*a*) Desired target ι profile and computed best matching, (*b*) $I(t)$, (*c*) $P_{\rm tot}$, (*d*) $\bar{n}(t)$.

for the three actuators are those shown in figures 18(*b*)–(*d*). The extremum seeking algorithm converges to a minimum in less than 20 iterations.

The second simulation case considers the initial poloidal flux ψ shown in figure 17(*b*) and the monotonic target ι profile with near zero shear near the axis shown in figure 19(*a*). Figure 19(*a*) compares the ι profile obtained by applying the extremum-seeking-based, optimal, open-loop control, with the target ι profile. The time evolutions for the three actuators are shown in figure 19(*b*)–(*d*). Figure 19(*a*) also shows the time evolution of the ι profile driven by these actuator waveforms. The extremum seeking algorithm converges to a minimum in less than 50 iterations.

The third simulation case considers the initial poloidal flux ψ shown in figure 17(*b*), and the reversed shear target ι profile shown in figure 20(*a*). Figure 20(*a*) shows the ι profile obtained by applying the extremum-seeking-based, optimal, open-loop control, and compares it with the target ι profile. The corresponding time evolutions for the three actuators are shown in figure 20(*b*)–(*d*). The time evolution of the ι profile driven by these actuator waveforms is also shown in figure 20(*a*). The extremum seeking algorithm converges to a minimum in less than 100 iterations.

All the figures depicting the actuator waveforms include the values of the associated components of θ obtained by the extremum seeking optimization algorithm. This allows for the distinction between the outcomes of the extremum seeking optimization and the optimal polynomical interpolation procedure. It is possible to note from some of these figures that

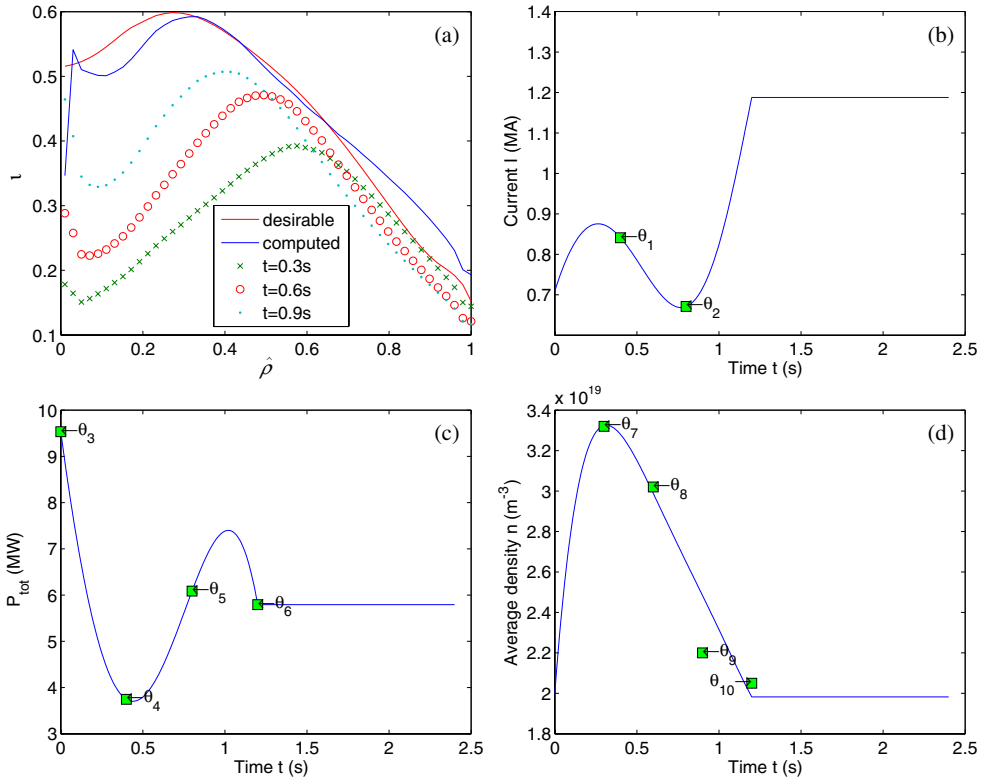

Figure 19. Simulation of extremum seeking optimal control: (*a*) Desired target ι profile and computed best matching, (*b*) $I(t)$, (*c*) P_{tot}, (*d*) $\bar{n}(t)$.

the optimal polynomical interpolation procedure avoids fitting some of the components of θ generated by the extremum seeking optimization algorithm in order to satisfy the value and rate constraints specified for the actuators.

6. Conclusions and future works

A multi-parameter, extremum-seeking, open-loop, optimal controller has been designed, and successfully tested in simulations, to match a desired ι profile within a predefined time window during the flattop phase of the tokamak discharge.

Three simulation cases based on target profiles of increasing complexity have been presented. The extremum-seeking procedure has shown to be effective to deal with an optimal control problem defined for a nonlinear PDE system subject to many constraints in its actuators. Based on the promising results obtained in the simulation study, it is anticipated that the scheme can play an important role in fusion plasma physics experiments at the DIII-D tokamak.

A simplified dynamic model describing the evolution of the poloidal flux, and therefore the ι profile, during the inductive phase of the discharge has been used. Alternatively, more accurate dynamic models for the prediction of the evolution of the poloidal flux profile can be implemented and used within the proposed Extremum Seeking optimal control scheme. Future work includes the use of predictive codes (CORSICA, CRONOS, PTRANSP, etc) for the design

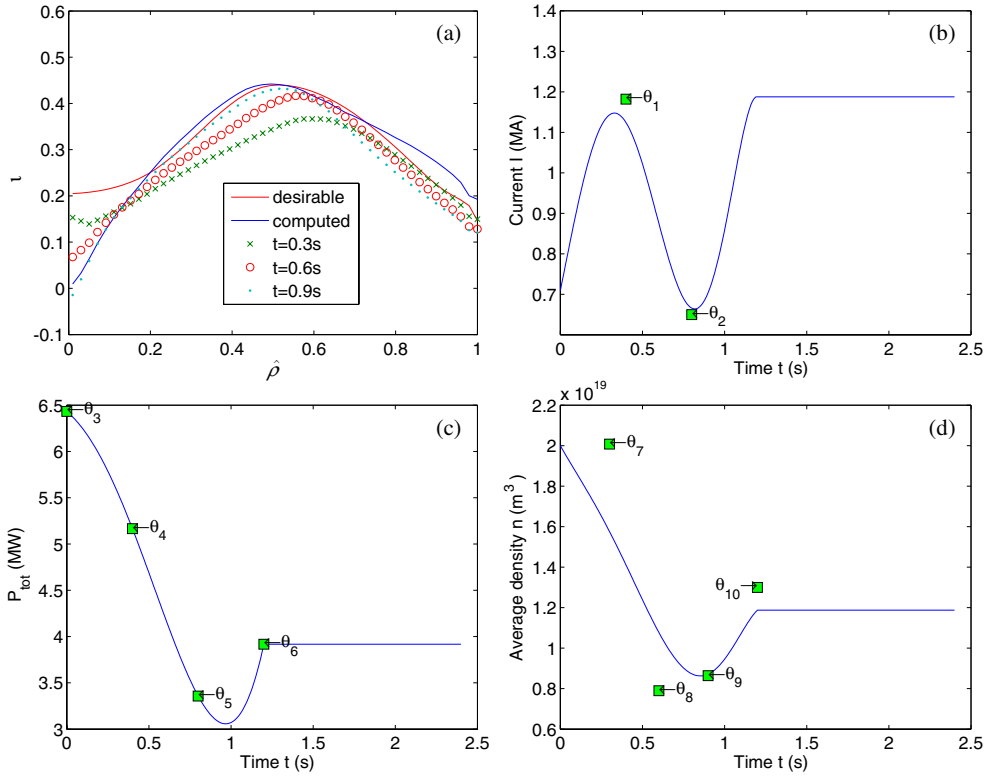

Figure 20. Simulation of extremum seeking optimal control: (*a*) Desired target ι profile and computed best matching, (*b*) $I(t)$, (*c*) P_{tot}, (*d*) $\bar{n}(t)$.

of open-loop, extremum-seeking-based, optimal controllers for current profile regulation, as well as the experimental testing of these controllers in the DIII-D tokamak.

Acknowledgments

This work was supported in part by a grant from the Commonwealth of Pennsylvania, Department of Community and Economic Development, through the Pennsylvania Infrastructure Technology Alliance (PITA), the NSF CAREER award program (ECCS-0645086), and General Atomics (DoE contract number DE-FC02-04ER54698). We gratefully acknowledge Dr Filippo Sartori from Euratom/UKAEA Fusion Association, Culham Science Centre, for providing the picture in figure 1.

Appendix

Without loss of generality, the static nonlinear block $J(\theta)$ in figure 16 is assumed to have a minimum at $\theta = \theta^*$, and to be of the form

$$J(\theta) = J^* + \frac{J''}{2}(\theta - \theta^*)^2, \tag{35}$$

where $J'' > 0$. Any C^2 function, $J(\theta)$, can be approximated locally by (35). The purpose of the extremum seeking algorithm is to make $\theta - \theta^*$ as small as possible, so that the output

$J(\theta)$ is driven to its minimum J^*. We note that $\hat{\theta}$ denotes the estimate of the unknown optimal input θ^*. In order to obtain a measure of the gradient information of the map $J(\theta)$, a probing signal $a\sin(\omega k)$, with $a > 0$, is fed into the plant (see (34)), i.e.

$$\theta = \hat{\theta} + a\sin(\omega k). \tag{36}$$

Let

$$\tilde{\theta} = \theta^* - \hat{\theta} \tag{37}$$

denote the estimation error. Thus,

$$\theta(k) - \theta^* = a\sin(\omega k) - \tilde{\theta}(k), \tag{38}$$

which, when substituted into (35), gives

$$J(k) \equiv J(\theta(k)) = J^* + \frac{J''}{2}(\tilde{\theta}(k) - a\sin(\omega k))^2. \tag{39}$$

Taking into account the trigonometric identity $2\sin^2(\omega k) = 1 - \cos(2\omega k)$, we can rewrite (39) as

$$J(k) = J^* + \frac{a^2 J''}{4} + \frac{J''}{2}\tilde{\theta}(k)^2 - aJ''\tilde{\theta}(k)\sin(\omega k) - \frac{a^2 J''}{4}\cos(2\omega k). \tag{40}$$

The high-pass filter, applied to $J(k)$, removes the constant terms and generates a filtered version of the cost functional (see (31)),

$$J_{\mathrm{f}}(k) = \frac{J''}{2}\tilde{\theta}(k)^2 - aJ''\tilde{\theta}(k)\sin(\omega k) - \frac{a^2 J''}{4}\cos(2\omega k), \tag{41}$$

where the information of the gradient of the map $J(\theta)$ is preserved. In particular, the second term plays a crucial role since it represents the gradient of the map multiplied by the perturbation introduced by the probing signal. The filtered cost functional is in turn demodulated by being multiplied by $\sin(\omega k)$ to generate (see (32))

$$\xi(k) = \frac{J''}{2}\tilde{\theta}(k)^2\sin(\omega k) - aJ''\tilde{\theta}(k)\sin^2(\omega k) - \frac{a^2 J''}{4}\cos(2\omega k)\sin(\omega k). \tag{42}$$

Applying again $2\sin^2(\omega k) = 1 - \cos(2\omega k)$, as well as the trigonometric identity $2\cos(2\omega k)\sin(\omega k) = \sin(3\omega k) - \sin(\omega k)$, we can rewrite (42) as

$$\begin{aligned}\xi(k) = &-\frac{aJ''}{2}\tilde{\theta}(k) + \frac{aJ''}{2}\cos(2\omega k) + \frac{a^2 J''}{8}(\sin(\omega k) - \sin(3\omega k)) \\ &+ \frac{J''}{2}\tilde{\theta}(k)^2\sin(\omega k).\end{aligned} \tag{43}$$

The low-pass filter, applied to $\xi(k)$, will remove the high-frequency terms (last three terms) and preserve the crucial term $-(aJ''/2)\tilde{\theta}(k)$ containing information on the gradient of the map $J(\theta)$. Therefore, we can write

$$\hat{\theta}(k) = \frac{-\gamma}{z-1}\xi(k) \approx \frac{\gamma}{z-1}\frac{aJ''}{2}\tilde{\theta}(k). \tag{44}$$

Taking into account definition (26) for the shift operator z, we can write (see (33))

$$\hat{\theta}(k+1) - \hat{\theta}(k) = \gamma\frac{aJ''}{2}\tilde{\theta}(k). \tag{45}$$

We note that $\hat{\theta}(k+1) - \hat{\theta}(k) = -(\tilde{\theta}(k+1) - \tilde{\theta}(k))$, and write

$$\tilde{\theta}(k+1) = \tilde{\theta}(k) - \gamma\frac{aJ''}{2}\tilde{\theta}(k) = \left(1 - \gamma\frac{aJ''}{2}\right)\tilde{\theta}(k). \tag{46}$$

Provided that $|1 - \gamma(aJ''/2)| < 1$ (a and γ are design parameters), this is a stable system. Thus, $\tilde{\theta} \to 0$, i.e. $\hat{\theta} \to \theta^*$.

For stability reasons the high-pass filter in figure 16 is designed as $0 < h < 1$. Since this is a discrete-time system, the modulation frequency ω is selected such that $\omega = \alpha\pi$, $0 < |\alpha| < 1$, and α is rational. Looking back at our elementary intuitive analysis, it is important to note that the approximations hold only when ω is large in a qualitative sense. The cutoff frequencies of the filters need to be lower than the frequency ω of the perturbation signal. These observations impose constraints and, at the same time, a relationship on ω and h. As an additional constraint, ω should not equal any frequency present in the measurement noise. The perturbation amplitude a needs to be small in order to make the steady-state output error also small. Given a, the adaptation gain γ needs to be small enough to satisfy the stability condition $|1 - \gamma(aJ''/2)| < 1$.

In this case, we are dealing with a multi-parameter extremum seeking procedure (the number of parameters n_p considered in this work is 10). Thus, we write

$$\theta(k) = \begin{bmatrix} \theta_1(k) \\ \vdots \\ \theta_{n_p}(k) \end{bmatrix}, \qquad \hat{\theta}(k) = \begin{bmatrix} \hat{\theta}_1(k) \\ \vdots \\ \hat{\theta}_{n_p}(k) \end{bmatrix}, \qquad \xi(k) = \begin{bmatrix} \xi_1(k) \\ \vdots \\ \xi_{n_p}(k) \end{bmatrix}. \tag{47}$$

The extremum seeking constants shown in figure 16 are written as $a = \mathrm{diag}([a_1 \cdots a_{n_p}])$, and $\gamma = \mathrm{diag}([\gamma_1 \cdots \gamma_{n_p}])$. In addition, we use the special compact notation where $\sin(\omega k)$ is a vector which denotes

$$\sin(\omega k) = \begin{bmatrix} \sin(\omega_1 k) \\ \vdots \\ \sin(\omega_{n_p} k) \end{bmatrix}. \tag{48}$$

It is convenient to use a separate frequency for each parameter tracking loop, following the guidelines given above. In general, using a single frequency to excite multiple parameter tracking loops leads to a greater coupling, and consequently to an increase in the design difficulty.

References

[1] Taylor T S *et al* 1997 Physics of advanced tokamaks *Plasma Phys. Control. Fusion* **39** B47–B73

[2] Murakami M *et al* 2006 Progress toward fully noninductive, high beta conditions in DIII-D *Phys. Plasmas* **13** 056106:1–056106:9

[3] Moreau D *et al* 2003 Real-time control of the q-profile in JET for steady state advanced tokamak operation *Nucl. Fusion* **43** 870–82

[4] Laborde L *et al* 2005 A model-based technique for integrated real-time profile control in the JET tokamak *Plasma Phys. Control. Fusion* **47** 155–83

[5] Suzuki T *et al* 2005 Recent RF experiments and application of RF waves to real-time control of safety factor profile in JT-60U *AIP Conf. (Park City, Utah, USA)* vol 787 pp 279–86

[6] Wijnands T *et al* 1997 Feedback control of the current profile on Tore Supra *Nucl. Fusion* **37** 777–91

[7] Barana O *et al* 2007 Feedback control of the lower hybrid power deposition profile on tore supra *Plasma Phys. Control. Fusion* **49** 947–67

[8] Moreau D *et al* 2006 New dynamic-model approach for simultaneous control of distributed magnetic and kinetic parameters in the ITER-like JET plasmas *Proc. 21th IAEA Fusion Energy Conf. (Chengdu, China)*

[9] Ferron J R *et al* 2005 Control of DIII-D Advanced Tokamak discharges *32nd EPS Conf. on Plasma Physics (Tarragona, Spain)* P 1.069

[10] Ferron J R *et al* 2006 Feedback control of the safety factor profile evolution during formation of an advanced tokamak discharge *Nucl. Fusion* **46** L13–7

[11] Ariyur K and Krstic M 2003 *Real-Time Optimization by Extremum Seeking Feedback* (Hoboken, NJ: Wiley)

[12] Ou Y, Schuster E, Luce T, Ferron J, Walker M L and Humphreys D A 2006 Towards model-based current profile control at DIII-D *Fusion Eng. Des.* **82** 1153–60
[13] Lao L L, St John H, Stambaugh R D, Kellman A G and Pfeiffer W 1985 Reconstruction of current profile parameters and plasma shapes in tokamaks *Nucl. Fusion* **25** 1611–22
[14] Ferron J R, Walker M L, Lao L L, St John H E, Humphreys D A and Leuer J A 1998 Real time equilibrium reconstruction for tokamak discharge control *Nucl. Fusion* **38** 1055–66
[15] Krstic M and Wang H-H 2000 Stability of extremum seeking feedback for general nonlinear dynamic systems *Automatica* **36** 595–601
[16] Rotea M 2000 Analysis of multivariable extremum seeking algorithms *Proc. American Control Conf. (Chicago, Illinois, USA)* vol 1, pp 433–7
[17] Binetti P, Ariyur K, Krstic M and Bernelli F 2003 Formation flight optimization using extremum seeking feedback *J. Guidance Control Dyn.* **26** 132–42
[18] Choi J-Y, Krstic M, Ariyur K and Lee J S 2000 Tuning of a combustion controller by extremum seeking: a simulation study *Proc. 39th IEEE Conf. on Decision and Control (Sydney, Australia)* vol 5 pp 5219–23
[19] Banaszuk A, Ariyur K, Krstic M and Jacobson C A 2004 An adaptive algorithm for control of combustion instability *Automatica* **40** 1965–72
[20] Wang H-H, Yeung S and Krstic M 2000 Experimental application of extremum seeking on an axial-flow compressor *IEEE Trans. Control Syst. Technol.* **8** 300–9
[21] Banaszuk A, Narayanan S and Zhang Y 2003 Adaptive control of flow separation in a planar diffuser *Proc. 41st Aerospace Sciences Meeting & Exhibit* pp AIAA-2003-0617
[22] Ariyur K and Krstic M 2002 Slope seeking and application to compressor instability control *Proc. IEEE Conf. on Decision and Control* vol 4 pp 3690–97
[23] Peterson K and Stefanopoulou A 2004 Extremum seeking control for soft landing of an electromechanical valve actuator *Automatica* **40** 1063–9
[24] Li Y, Rotea M A, Chiu G T-C, Mongeau L G and Paek I-S 2005 Extremum seeking control of a tunable thermoacoustic cooler *IEEE Trans. Control Syst. Technol.* **13** 527–36
[25] Wang H-H, Krstic M and Bastin G 1999 Optimizing bioreactors by extremum seeking *Int. J. Adaptive Control Signal Process.* **13** 651–9
[26] Choi J-Y, Krstic M, Ariyur K and Lee J S 2002 Extremum seeking control for discrete-time systems *IEEE Trans. Automatic Control* **47** 318–23
[27] Franklin G F, Powell J D and Workman M L 1997 *Digital Control of Dynamic Systems* (Reading, MA: Adison-Wesley) 3rd edn
[28] Franklin G F, Powell J D and Emami-Naeini A 2005 *Feedback Control of Dynamic Systems* (Englewood Cliffs, NJ: Prentice Hall) 5th edn